ARTICLE

Growth and Optical Properties of Gold Nanoshells Prior to the Formation of a Continuous Metallic Layer

Thomas C. Preston and Ruth Signorell*

Department of Chemistry, University of British Columbia, 2036 Main Mall, Vancouver, BC V6T 1Z1, Canada

ABSTRACT The growth and optical properties of incomplete gold layers on silica particles (229 nm) are studied using visible/near-infrared spectroscopy and transmission electron microscopy. The gold particles that eventually coalesce to form a continuous gold layer are found to have droplet-like shapes. The optical properties of these systems are different from those of complete gold nanoshells. Using the discrete dipole approximation, it is found that the plasmon modes of such systems should exhibit two bands: one from 500—600 nm ("high energy") and the other from 600—800 nm ("low energy"). The calculations show that, for increasing coating density of the droplet-like particles, the lower energy band (i) becomes stronger relative to the higher energy band and (ii) is red-shifted. Both of these trends are found in the spectra of the prepared particles. Furthermore, the observed plasmon bands fall within the limits established by the model.

KEYWORDS: gold nanoparticles · gold nanoshells · plasmonics · discrete dipole approximation

Gold nanoshells, particles that consist of a spherical dielectric core coated with a concentric layer of gold, have become ubiquitous in applications such as thermal therapy,[1−6] biological imaging,[3,7−9] controlled drug release,[5,10−12] and surface-enhanced spectroscopy.[13−16] The strong dependence of their plasmon modes on the gold shell thickness allows for great control over how these particles absorb and scatter electromagnetic radiation.[17−19] Specifically, large extinction cross sections at wavelengths in the near-infrared (NIR), important for biological applications, are easily demonstrated.

One of the most popular approaches to construct gold nanoshells involves attaching small gold particles to the surfaces of silica cores and, subsequently, using these sites as nuclei to seed shell growth when a gold salt is reduced in their presence.[18,20] In this type of a synthesis, it should be possible to control the shell thickness by adjusting the amount of reducible salt present in solution and, as this thickness influences the plasmon modes of the particle,[18] engineer the particle's electromagnetic response. Ideally, this approach should be guided by a theoretical understanding of the behavior of the spectra for such a particle. By using the analytical solution to the diffraction of electromagnetic radiation by a coated sphere, this is indeed possible.[21] These results have been discussed in detail elsewhere.[17−19] The general trend can be summarized as follows: when a shell's thickness is less than the radius of the sphere that it coats—and all other factors are held constant—a blue shift in the particle's plasmon band position will occur as the shell's thickness is increased.

Of course, this is only true if a uniform gold layer is present on the surface of the dielectric core.[22] Given the manner in which shell growth takes place, one would suspect that this is not always the case. Certainly, there must exist situations where shell formation is incomplete and only islands of gold are present on the surface of the core (*e.g.*, when insufficient reducible salt is added during the growth process). The illustration in Figure 1 compares an incomplete with a complete nanoshell. In the former case (Figure 1a), the electromagnetic response of a particle cannot be described by the model of a sphere coated with a layer of constant thickness.

In this report, we examine how the visible and NIR spectra of gold nanoshells behave as a function of the concentration of gold salt added during shell growth. Specifically, we focus our attention on the region where shell formation is incomplete and model how the spectra depend on the morphology of gold present on the surface of the silica sphere. Transmission electron microscopy (TEM) is used to examine the vari-

*Address correspondence to signorell@chem.ubc.ca.

Received for review July 28, 2009 and accepted September 18, 2009.

Published online September 28, 2009.
10.1021/nn900883d CCC: $40.75

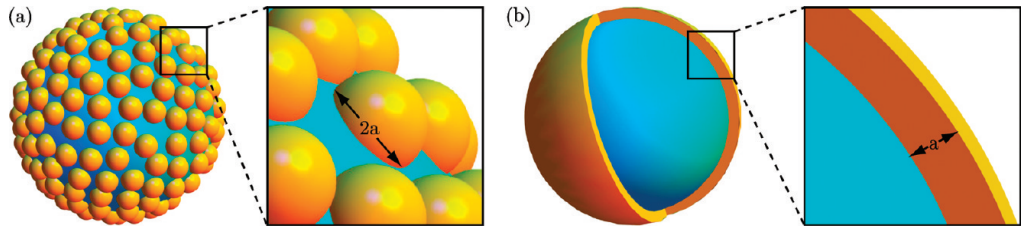

Figure 1. Parameter a is used to either represent (a) the gold particle radius or (b) the shell thickness.

ous particle surfaces and determine the parameters which are used in the model. From these images, we also discuss the processes through which shell growth occurs in this regime of incomplete shell formation.

RESULTS AND DISCUSSION

Modeling of Optical Properties. Our study focuses on particles composed of silica cores onto which incomplete gold layers have been grown. As these layers originate from small, roughly spherical seed particles, early stages of growth most likely result in enlarged versions of these precursors (as shown in Figure 1a). When modeling the optical properties of these gold structures, the shape of the individual particles is described as spheres, hemispheres, or droplet-like particles—an intermediate between the spherical and hemispherical shape. The study of the droplet-like shape is motivated by the particles observed in TEM images (see the Characterization of Particles by TEM section). While the optical properties of spherical particles have been extensively studied,[23−26] those of hemispherical particles have only been examined in a few cases.[27] As the number of individual gold particles on any given silica sphere is quite large, a numerical approach to describe the optical properties would be computationally unfeasible. Therefore, we examine either small clusters of spherical or hemispherical particles. This may appear to be a limitation, but it is actually possible to determine most of the key properties and spectral trends of these larger systems using only a small number of particles.

The electromagnetic responses of gold structures considered here are modeled using the discrete dipole approximation (DDA).[28,29] The density of dipoles used was either 27 dipoles/nm^3 (when the radii of the structures were 10 nm) or 8 dipoles/nm^3 (when the radii of the structures were 20 nm). The dielectric function of gold is taken from a table.[30] The refractive index of the medium that surrounds the hemispheres is taken to be nondispersive and set to 1.33 (water). The silica surface is ignored in these calculations. This simplification slightly shifts calculated resonances to shorter wavelengths.[31,32] Given the large range of wavelengths over which the experimental resonances are found and the small difference in refractive index between the silica core ($n_{silica} = 1.44$)[33] and water, this approximation is satisfactory.

The clusters of spheres and hemispheres we consider can be classified according to their point groups. Their dimensions are typically much smaller than the wavelength of light impinging on them. Therefore, the electric dipole active modes dominate the spectra. The irreducible representations of these modes are used to label the peaks in the extinction spectra. This approach to label plasmon modes has been taken previously by Mayergoyz *et al.*[34] and was used when dealing with so-called plasmonic molecules.[35,36]

Single Sphere or Hemisphere. The optical properties of individual gold spheres are well-known[23] and are only included here for comparison with those of a hemisphere. Figure 2a shows the location of the maximum of the dipole mode, *p*, as a function of sphere radius. Figure 2c shows a sample spectrum for a constant radius of $a = 10$ nm. The maximum of the dipole mode shifts to longer wavelengths as the radius increases.

On the basis of the point group of a hemisphere ($C_{\infty v}$), of the three electric dipole modes, one is nondegenerate (Σ^+) and two are degenerate (Π). Figure 2b shows the location of the extinction maximum of these modes as a function of the hemisphere radius, *a*. An example of the spectra associated with these two modes for a constant radius $a = 10$ nm is given in Figure 2d. It turns out that, at their respective maxima, the extinction cross section of the Π modes is about seven times larger than that of the Σ^+ mode. This, combined with the fact that for a randomly oriented hemisphere both Π modes will be active, means that the spectra of the gold hemispheres will essentially be dominated by this lower energy mode.

A Pair of Spheres or Hemispheres. A pair of spheres belongs to the $D_{\infty h}$ point group. Figure 3a shows the variables *s* and *a*, which describe the system and the orientation of the polarization that excites the nondenergate mode (Σ_u^+) and the doubly degenerate modes (Π_u). Figure 3b,c shows the maxima of the dipole modes as a function of the shortest distance between the surfaces of two spheres, *s*, for two different radii $a = 10$ and 20 nm, respectively. Examples of the extinction spectra for $s = 1$ nm are shown in Figure 3d,e, respectively.

With decreasing separation, *s*, the Π_u modes show little change in their extinction maxima (small blue shift) while the Σ_u^+ modes strongly red shift. For identical *s*, the Σ_u^+ mode of the larger spheres ($a = 20$ nm, Figure 3c) is shifted to longer wavelengths than that of the small spheres ($a = 10$ nm, Figure 3b). We also note that the Σ_u^+ modes have much larger extinction cross sections than the Π_u modes. However, in an orienta-

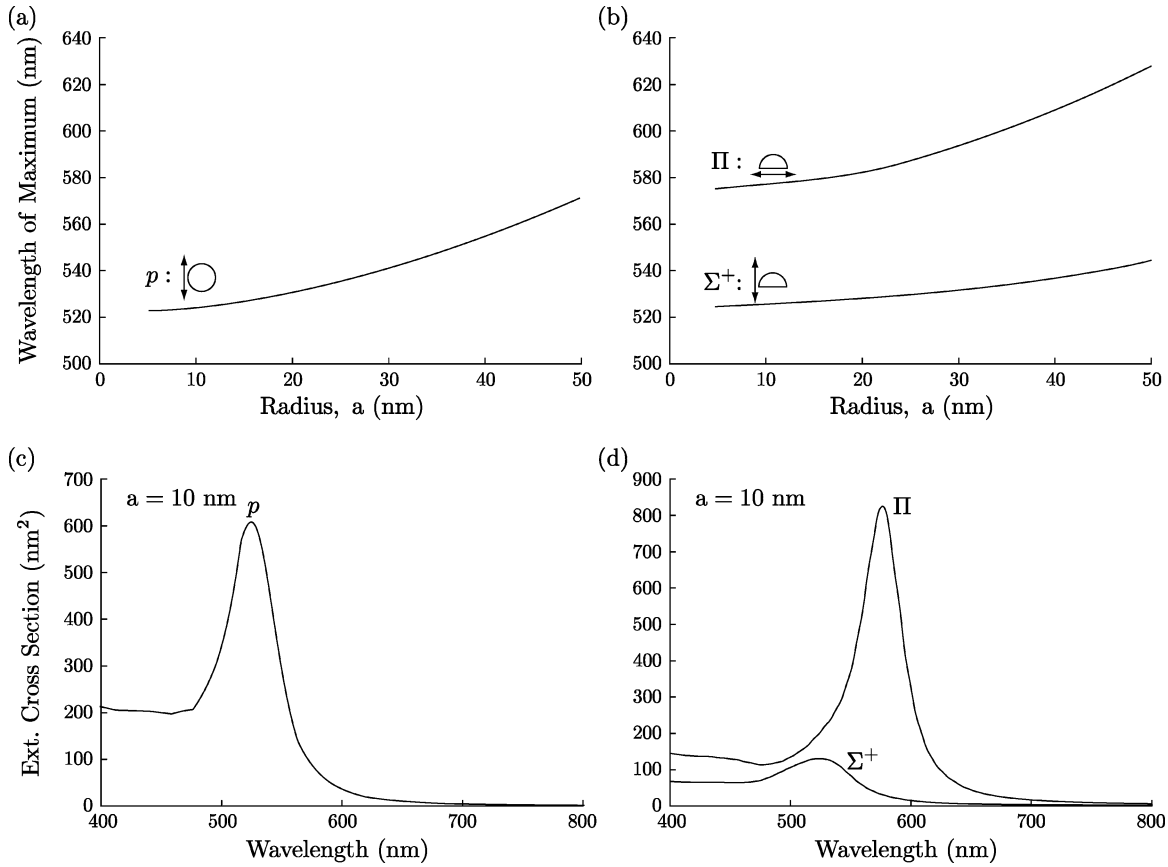

Figure 2. (a) Location of the plasmon extinction maximum as a function of sphere radius, *a*. (b) Location of the plasmon extinction maximum as a function of hemisphere radius, *a* (polarization of incident electric field is indicated with double-sided arrows). (c) Sphere spectrum for *a* = 10 nm, and (d) hemisphere spectra for two polarizations for *a* = 10 nm.

tionally averaged sample, both Π_u modes are active and their relative contribution thus increases.

For a pair of hemispheres, we assume that the hemispheres lie on a flat surface. Figure 4a shows the orientation and parameters of the two hemispheres used in these calculations. This configuration belongs to the C_{2v} point group, and all three electric dipole modes will be nondegenerate. Figure 4a shows the orientation of the polarization that excites these modes together with their labels. Figure 4b,c shows the maxima of the dipole modes as a function of separation, *s*, for radii of *a* = 10 and 20 nm, respectively. When the spacing, *s*, is decreased, we observe a large red shift in the B_2 modes and much smaller blue shifts in the B_1 and A_1 modes. Similar to the case of the paired spheres, the red shift is more pronounced for larger particle radii. Figure 4d,e shows the spectra of these modes for a fixed separation *s* = 1 nm and radii of *a* = 10 and 20 nm, respectively. Similar to the case of a single hemisphere (Figure 2d), the lowest energy mode—here it is B_2—possesses the largest extinction cross section and should be readily observable. However, this mode will not be as dominant in an orientationally averaged spectrum as the Π mode of the isolated hemisphere.

In relation to each other, the spectra of the paired sphere (Figure 3) and hemisphere (Figure 4) are very similar, although when spacing and radii are equal, the low energy B_2 mode of the hemisphere system is found at longer wavelengths than the low energy Σ_u^+ mode of the spherical system. Note that a smaller peak associated with an electric quadrupole moment is visible at shorter wavelengths in the traces that contain the Σ_u^+ mode and B_2 mode in Figure 3 and Figure 4, respectively.

A Series of Spheres or Hemispheres. For either spheres or hemispheres, the difference in spectra between the isolated (Figure 2) and paired cases (Figures 3 and 4) is quite significant. Therefore, it is worthwhile to investigate the effects of placing additional spheres or hemispheres in the series. This gives an impression of how quickly the spectra converge. For either set of objects, the most convenient way to proceed is by placing all of them along the same axis and maintaining an equal spacing, *s*, between neighboring members of the series (and for hemispheres maintaining identical orientation). When this is done, the $D_{\infty h}$ and C_{2v} symmetries of the paired cases are retained for the spheres and hemispheres, respectively. For the spheres, physical intuition tells us that this will represent a limit on the longest observable wavelength for such a cluster (*i.e.*, when compared to other systems with the same number of spheres

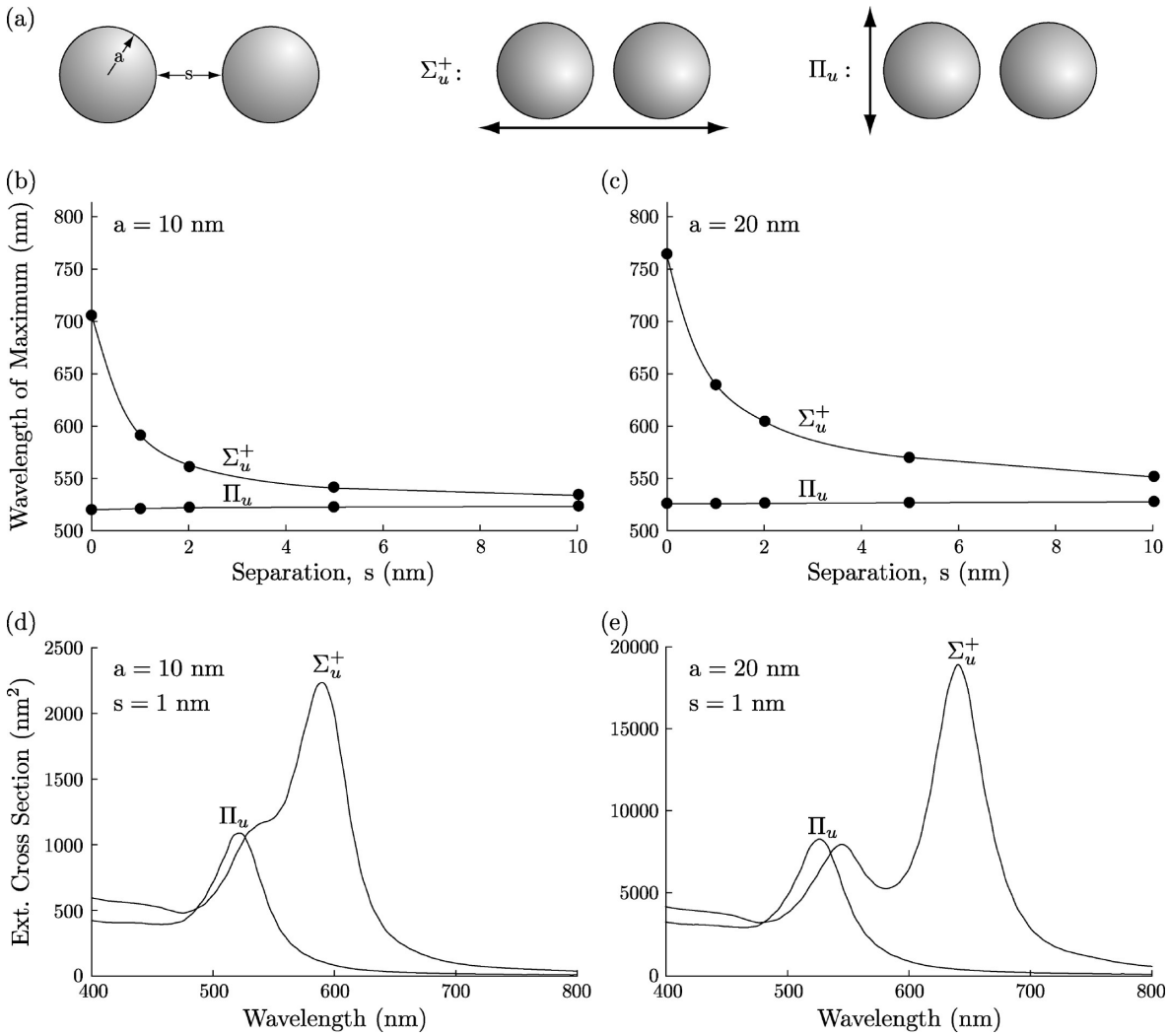

Figure 3. Location of the plasmon extinction maximum for a pair of spheres (shown in (a)) as a function of sphere separation, *s*, for (b) *a* = 10 nm and (c) *a* = 20 nm. Traces (d) and (e) show spectra of these modes at a separation, *s*, of 1 nm and a radius, *a*, of 10 and 20 nm, respectively. The definition of the modes is shown in (a).

and where the shortest spacing between any two spheres is not less than *s*).

We shall only examine the Σ_u^+ mode in the case of spheres and the B_2 mode in the case of hemispheres as these were found to be the strongest in the paired case and the only modes whose maxima changed significantly (red-shifted) when coupled. Figure 5a,b shows the location of these modes as the number of objects in the series increases. With each new object that is added to the series, a red shift occurs. However, the magnitude of this shift also decreases as more objects are added. Although neither of the series completely converges, in both cases after $N = 4$, the red shift is quite minor. The red shift in the hemisphere case is more pronounced than that of the case of the sphere. Finally, the maxima of the modes not shown here (B_1, A_1, and Π_u) do not change significantly when additional objects are added to the series.

Cluster of Four Spheres or Hemispheres. In a situation where spheres or hemispheres are randomly distributed on a surface, such as those that are considered in the Characterization of Particles by TEM section, a cluster of individual particles might be a better representation than a series of particles. To gain some appreciation of this, we examine two such cases: those of four spheres (Figure 6) and four hemispheres (Figure 7). The point groups of these arrangements are D_{4h} and C_{4v}, respectively. As *s* decreases, both the spherical and hemispherical configurations have a strong red shift in their lowest energy mode (E_u and *E*, respectively). However, the absolute shift is not as large as in the linear case for $N = 4$ (Figure 5). More importantly, the overall appearance of the spectra in Figures 6 and 7 is very similar to the spectra of the respective pairs in Figures 3 and 4. Note again that, similar to the paired sphere and hemisphere cases, a smaller peak associated with an electric quadrupole moment is visible at shorter wavelengths in the traces that contain the E_u mode and *E* mode in Figures 6 and 7, respectively.

Droplet-like Structure. Figure 8 shows the extinction maxima of the two modes of droplet-like gold par-

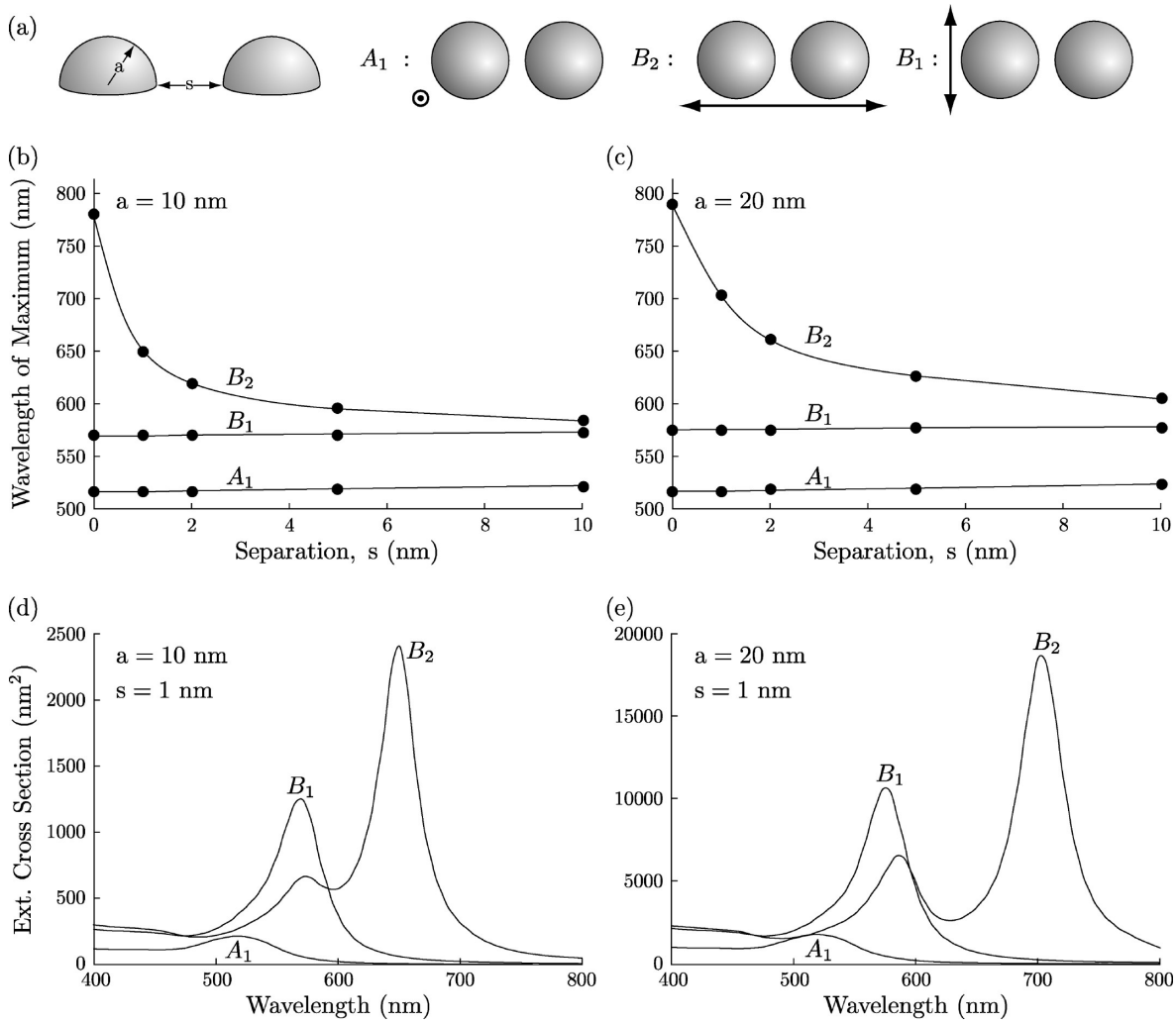

Figure 4. Location of the plasmon extinction maximum for a pair of hemispheres (shown in (a)) as a function of hemisphere separation, *s*, for (b) *a* = 10 nm and (c) *a* = 20 nm. Traces (d) and (e) show spectra of these modes at a separation, *s*, of 1 nm and a radius, *a*, of 10 and 20 nm, respectively. The definition of the modes is shown in (a).

ticles (see inset for details) with a radius $a = 10$ nm and a varying base height, b. An axis showing the contact angle for the a-to-b ratios is also plotted. The maximum wavelength of the dominant Π mode increases monotonically between the spherical ($b = 10$ nm) and hemispherical limits ($b = 0$ nm). Therefore, the hemispherical and spherical clusters which we have considered earlier represent, as an approximation, upper and lower bounds on the maximum wavelength for equivalent clusters made up of these droplet-like structures.

Summary of Optical Properties. The systematic calculations performed here tell us where to expect resonances and what their relative strengths are. For a closely spaced system of particles ($s < 4$ nm), extinction maxima are much more sensitive to changes in spacing than changes in particle radii (*i.e.*, within this region, changing the separation will have a greater effect on the maxima location than an identical change to the radii). Independently of the arrangement of the individual particles, there are generally two types of modes: "high energy" modes from 500 to 600 nm and "low energy" modes from 600 to 800 nm. Therefore, for a system of particles randomly distributed across a surface, two plasmon bands should be observable in the extinction spectrum—one comprising the higher energy modes and the other the lower energy modes. Within the context of the plasmon hybridization model,[37] this is simply the splitting of the uncoupled plasmon resonance into higher and lower energy modes.

The comparison of the results for two spheres or hemispheres (Figures 3 and 4) with those of four spheres or hemispheres (Figures 6 and 7) illustrates that the number of high energy modes goes from two to one and the number of low energy modes goes from one to two (taking into account the degeneracy of some of the modes present). These two cases are examples of a more general phenomenon: as the packing density of randomly placed gold objects on a surface increases, the lower energy band will increase in strength at the expense of the higher energy band. The other effect of the increasing density is that the low energy band red shifts.

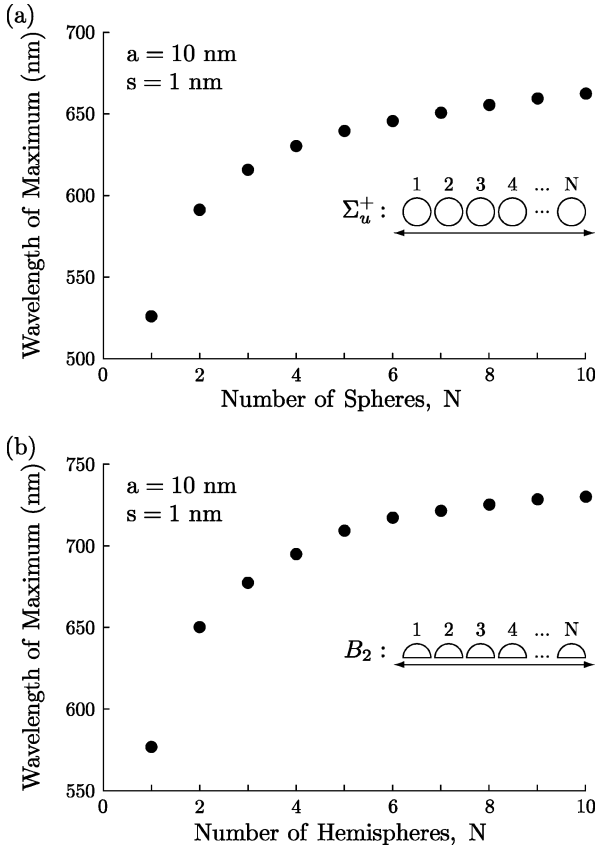

Figure 5. Location of the plasmon extinction maximum for (a) the Σ_u^+ mode as the number of spheres in a series is increased (or the *p* mode when the number of spheres is equal to 1) and (b) the B_2 mode as the number of hemispheres in a series is increased (or the Π mode when the number of hemispheres is equal to 1). The spacings between the spheres or hemispheres in the series and radii were held constant at 1 and 10 nm, respectively.

Characterization of Particles by TEM. Figure 9 shows TEM images for nanoshell precursors where increasing amounts of the gold salt solution have been reduced in their presence. We first describe the differences between the images qualitatively. For low concentrations of reducible gold salt solution, isolated gold particles are found on the silica surface (Figure 9a−e). As the concentration of reducible salt is increased, these particles grow in diameter, coalesce, and eventually form a surface better described as being continuous (Figure 9f−i). This suggests a lower limit on the thickness of a completed nanoshell in the range of 11 to 16 nm (the thickness of the gold shells for the particles in Figure 9f,i, respectively).

During the growth process of the individual gold particles, the most pronounced change appears to occur from Figure 9a to b. Here, not only does the size of the gold particles on the surface increase, as one would expect, but, as is evident by inspection, the number of gold particles greatly decreases. Furthermore, there are large areas of the silica surface that would have contained small gold particles in Figure 9a but are bare in Figure 9b. These observations suggest that the larger particles in Figure 9b do not originate from single seed particles but rather encompass several of these seed particles.

Two-dimensional TEM images can be a limitation in elucidating the three-dimensional structure of particles. However, the spherical silica surface onto which the particles are bound allows one to view all orientations of the gold particles. In Figure 9b,c, the gold particles on the outer edge of the silica spheres, for example, show that the individual particles have droplet-like shapes. This morphology lies somewhere between the spherical and hemispherical shapes discussed in the Modeling of Optical Properties section. The contact angle of these particles could be measured from the TEM images, and values of 125 ± 8° (Figure 9b) and 130 ± 9° (Figure 9c) were obtained. If we assume that only dispersion forces between gold and silica determine this contact angle, we can calculate this value from Young's equation.[38] For that purpose, we used the surface energies of gold $\gamma Au = 1130$ mJ m^{-2},[39] silica $\gamma Si = 31$ mJ m^{-2},[40] and the interface energy $\gamma Au,Si = \gamma Au + \gamma Si - 2\sqrt{(\gamma Au\, \gamma Si)} = 787$ mJ m^{-2}. This leads to a calculated contact angle of 132°, which is in reasonable agreement with the experimental values.

Droplet-like growth has been discussed previously for gold growing on a flat, doped polypyrrole surface.[41] While the sample preparation in that work was quite different from ours (*e.g.*, gold films were grown by vapor deposition), the surface energies of that system were very similar, suggesting that general dispersion forces play an important role in determining gold particle morphology here, as well. The contact angle in that case (128°) was similar to our measurements. In contrast to our study, however, the contact angle could not be measured directly but was extrapolated to fit X-ray photoelectron spectroscopy (XPS) measurements.

Table 1 quantifies the average radius, *a*, of the gold particles found on the silica surfaces and the percentage of the silica core surface they cover. These data were obtained from TEM images. For cases where the edges of two particles were touching, this was measured and counted as two separate particles. Alternatively, when the coverage of the silica surface by gold was high, the gold hemisphere radius was obtained from the difference between the total nanoshell diameter and the silica core diameter (see Figure 1b). Where both of these results could be applied (Figure 9d,e), results determined in either manner were in agreement. For the situation depicted in Figure 9f−i, only the second method was applicable and the radius *a* is better interpreted as being the nanoshell thickness. When determining the percentage of surface coverage, only the portion of the surface near the center of a silica sphere on a TEM image was used so that the gold par-

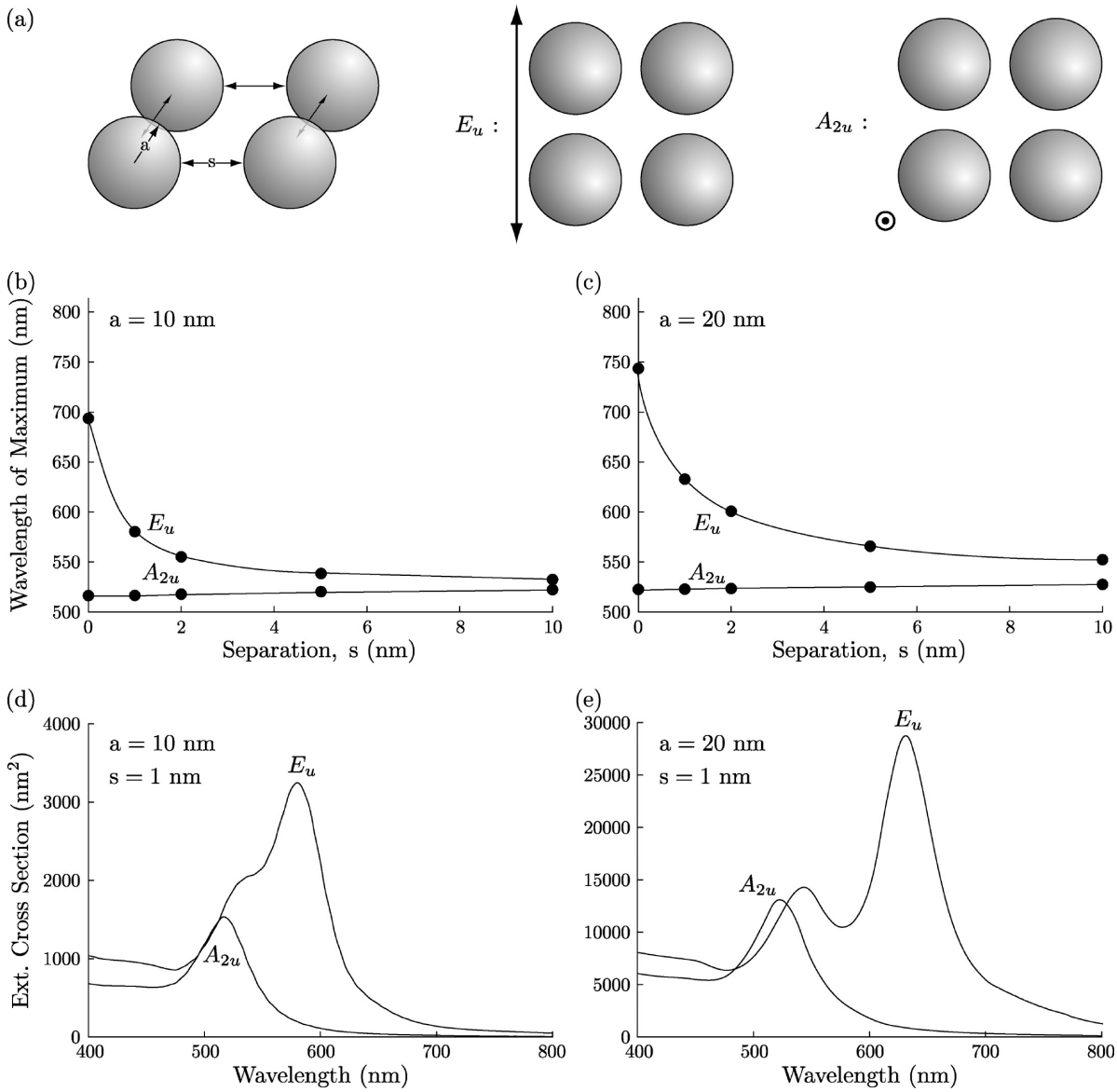

Figure 6. Location of the plasmon extinction maximum for four spheres (shown in (a)) as a function of sphere separation, *s*, for (b) *a* = 10 nm and (c) *a* = 20 nm. Traces (d) and (e) show spectra of these modes at a separation, *s*, of 1 nm and a radius, *a*, of 10 and 20 nm, respectively. The definition of the modes is shown in (a).

ticles did not obscure uncoated area and cause an overestimation of the surface coating. The nearest neighbor distance between two particles, *s*, was not measured directly but instead calculated using the measured coverage of silica by gold. This was done by preparing a plot of area covered *versus* nearest neighbor distance using values of area and nearest neighbor distance calculated by randomly placing circles with radii of 80 units on a 8000 × 8000 unit grid. In order to avoid artifacts introduced by not using an infinite grid, circles within 1600 units of the grid edge were not included in these calculations.

Characterization of Particles by UV−Vis−NIR Spectroscopy. The UV−vis−NIR spectra of the prepared particles are shown in Figure 10, and the positions of the high energy (P_{high}) and low energy (P_{low}) plasmon bands, observed as maxima or shoulders, are indicated, as well. These values are also listed in Table 1. In Figure 10a, the absence of any observable plasmon peak is most likely due to the small dimensions of the gold particles (Figure 9a), the plasmon oscillations of which will be heavily damped. In Figure 10f−i, the fraction of silica covered by gold is larger than that of the densest possible packing of circles on a flat surface (hexagonal packing, ~0.91). Therefore, overlap between gold particles is significant, and the spectra are essentially those of completed nanoshells. In Figure 10b−e, we observe a double band structure consisting of P_{low} and P_{high}. In addition, the low energy band, P_{low}, strongly red shifts from trace b to e. The high energy band, P_{high}, exhibits only a minor shift. These spectra correspond to particles where complete shells have yet to form. To explain the

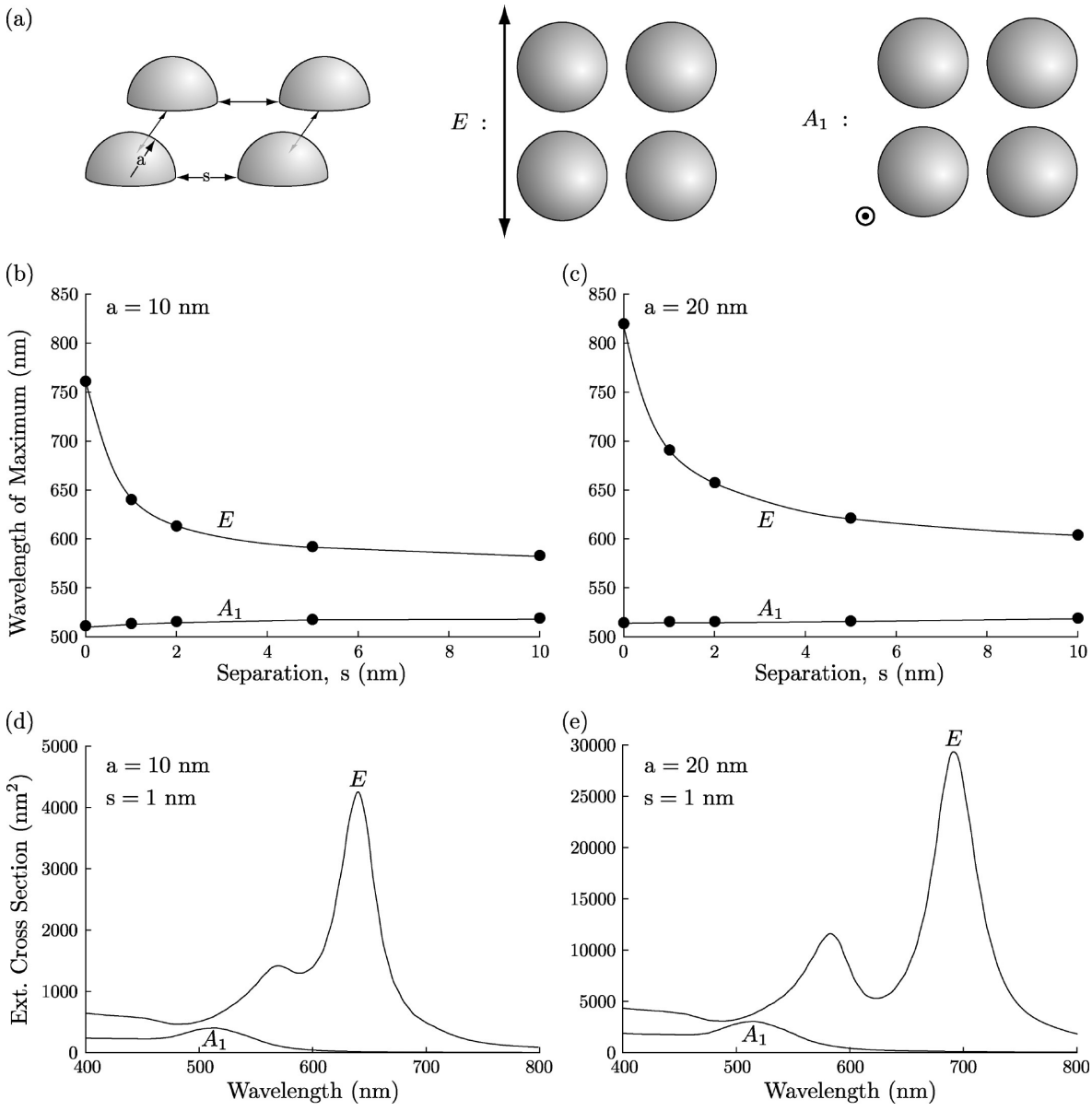

Figure 7. Location of the plasmon extinction maximum for four hemispheres (shown in (a)) as a function of hemisphere separation, *s*, for (b) *a* = 10 nm and (c) *a* = 20 nm. Traces (d) and (e) show spectra of these modes at a separation, *s*, of 1 nm and a radius, *a*, of 10 and 20 nm, respectively. The definition of the modes is shown in (a).

origin of this red shift, along with the observed double structure, we use the data extracted from the TEM images (Table 1) together with the results from the Modeling of Optical Properties section.

The radii of the discrete gold particles observed in Figure 9b−e are listed in Table 1. Within the uncertainties, these values are all ~10 nm. Despite this similarity in size, we observe a strong red shift of P_{low}. In contrast to this nearly constant radius, the fraction of the silica surface covered by gold increases from 0.31 to 0.79 (Table 1). This obviously affects the spacing between gold particles and corresponds to a decrease in the nearest neighbor distance between particles, *s*, from about 3.49 nm to essentially 0. This indicates that interparticle plasmon coupling between the gold structures is strong and causes the observed red shift.

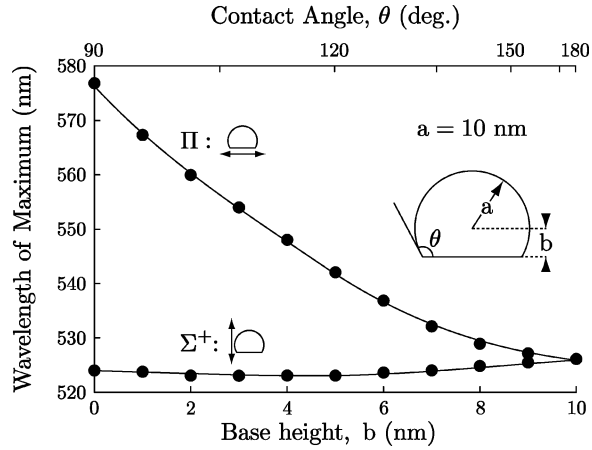

Figure 8. Location of plasmon extinction maxima as a function of base height, *b*, for a droplet-like structure of radius *a* = 10 nm.

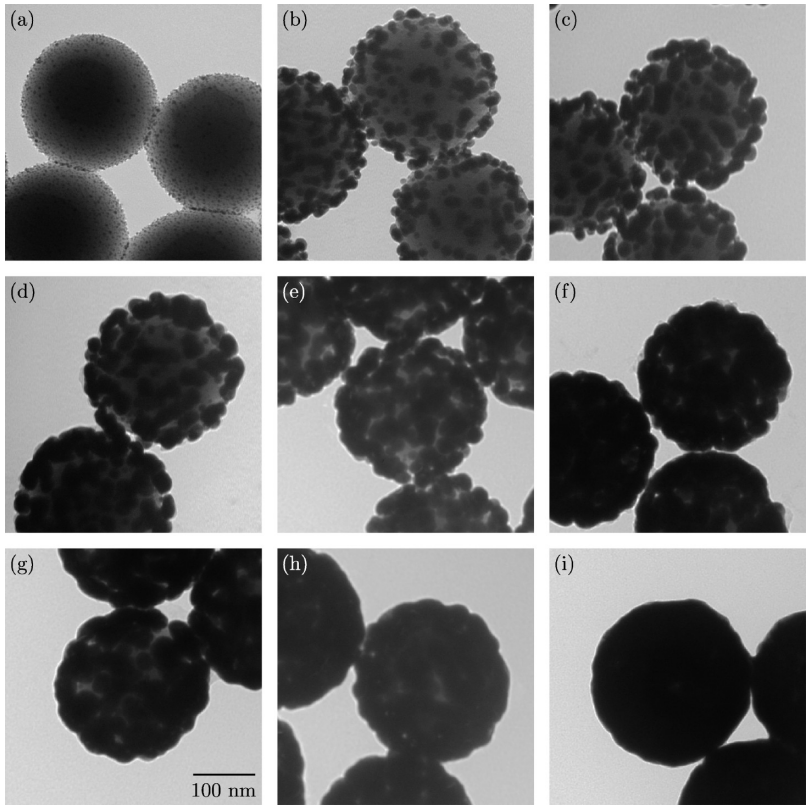

Figure 9. TEM images for prepared nanoshells. Volume of stock $HAuCl_4/K_2CO_3$ added during coating procedure: (a) 0 mL, (b) 0.25 mL, (c) 0.50 mL, (d) 0.75 mL, (e) 1.00 mL, (f) 1.25 mL, (g) 1.50 mL, (h) 1.75 mL, and (i) 2.00 mL. Corresponding UV–vis–NIR extinction spectra are shown in Figure 10.

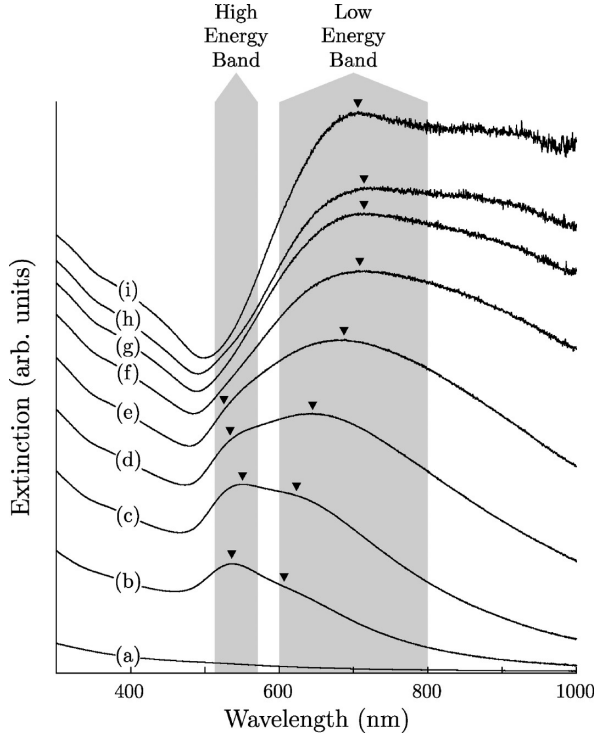

Figure 10. UV–vis–NIR extinction spectra for nanoshell solutions. Volume of stock $HAuCl_4/K_2CO_3$ added during coating procedure: (a) 0 mL, (b) 0.25 mL, (c) 0.50 mL, (d) 0.75 mL, (e) 1.00 mL, (f) 1.25 mL, (g) 1.50 mL, (h) 1.75 mL, and (i) 2.00 mL. The locations of the high energy (P_{high}) and low energy (P_{low}) plasmon bands are indicated using arrows. Corresponding TEM images are shown in Figure 9.

The high and low energy band description developed in the summary portion of the Modeling of Optical Properties section provides an adequate explanation as to the observed double structure. As predicted for spherical and hemispherical objects placed on a surface, two distinct bands appear. With increasing coating density, the lower energy band (i) red shifts and (ii) increases in strength relative to the higher energy band. Note again that the same holds for the droplet-like particles as they represent an intermediate between spherical and hemispherical objects. In Figure 10b–e, these two bands are always observed as a maximum or a shoulder. Initially, the high energy band, P_{high}, appears as the main peak, while the low energy band, P_{low}, is a shoulder (Figure 10b,c). As the coating density of gold on silica increases, P_{high} becomes a shoulder and P_{low} develops to become the main peak (Figure 10d,e). Not only are the two predicted bands observed—within the correct range of wavelengths predicted from the calculations—but the proper trend is also found: P_{low} strongly red shifts from 607 nm in Figure 10b to 684 nm in Figure 10e and becomes stronger than P_{high}, which only shifts by a minor amount.

For systems containing large numbers of closely spaced, randomly distributed plasmonic particles, predicting the precise location of extinction maxima with DDA is difficult due to computational limitations. However, the fact that the bands in Figure 10b–e fall within the limits established in the Modeling of Optical Properties section for gold particles characterized by the TEM images provides clear evidence that coupling between the latter is responsible for the observed double structure and intensity distribution.

SUMMARY

The initial growth of gold nanoshells occurs through a combination of gold being plated onto the adsorbed seed particles and a process where these seed particles evolve into a smaller number of larger particles on the silica surface. These particles have a droplet-like shape. Prior to the formation of a continuous gold layer on the silica core, such incomplete nanoshells exhibit high (500–600 nm) and low (600–800 nm) energy bands. Modeling shows that this is the result of interparticle plasmon coupling that occurs mainly between nearest neighbor gold particles adsorbed to the silica surfaces. Model clusters of hemispheres and spheres establish upper and lower bounds for the wavelengths

TABLE 1. Parameters Extracted from TEM Images (see Figure 9)

label in Figures 9 and 10	volume of gold salt solution (mL)	particle radius or shell thickness, *a* (nm) (see Figure 1)	fraction of silica surface covered by gold	nearest neighbor distances between gold particles (nm)	wavelength (nm) of plasmon bands P_{high}, P_{low}
b	0.25	9 ± 3	0.31 ± 0.11	3.4 ± 1.1	536, 607
c	0.50	11 ± 3	0.51 ± 0.07	1.5 ± 1.4	550, 625
d	0.75	14 ± 6	0.66 ± 0.13	0.2 ± 0.2	535, 644
e	1.00	10 ± 5	0.79 ± 0.14	0	527, 684
f	1.25	11 ± 5	0.94 ± 0.05	0	−, 710
g	1.50	17 ± 5	0.93 ± 0.06	0	−, 715
h	1.75	16 ± 3	0.98 ± 0.03	0	−, 715
i	2.00	16 ± 6	0.99 ± 0.01	0	−, 705

of these bands. The experimental results for incomplete nanoshells with discrete gold particles fall within the predicted limits.

The present results allow for a simple identification of the incomplete growth of nanoshells by UV−vis−NIR spectroscopy. Incomplete growth is an issue in systems where the creation of very thin gold layers is desired. Furthermore, our study provides an explanation as to the origin of the observed optical properties of these systems.

EXPERIMENTAL SECTION

Synthesis. The detailed preparation of the gold nanoshells is described in the Supporting Information. Briefly, 229 ± 11 nm diameter silica cores were prepared using the Stöber method.[42] Their surface was functionalized with 3-aminopropyltrimethoxysilane.[43] Gold particles (2.4 ± 0.5 nm diameter)[44,45] were adsorbed on the surface of these aminated silica particles. Two hundred microliters of this colloid was mixed with various volumes of a gold salt solution (1.5 mM $HAuCl_4$ with 1 mg/mL K_2CO_3; see Table 1 for volumes) and made up to 4 mL with H_2O. Gold was reduced by adding 10 μL of formaldehyde.[20]

Characterization. Transmission electron microscope (TEM) images were collected using a Hitachi H7600 TEM. Samples were prepared by placing 10 μL of the solution of interest onto the surface of a Formvar/carbon 200 mesh, copper grid (Ted Pella, Inc.). The solvent was then left to evaporate. Ultraviolet−visible−near-infrared (UV−vis−NIR) spectroscopy was performed using a Varian Cary 50 UV−vis spectrophotometer. All samples were dispersed in water and held in quartz cells during analysis.

Acknowledgment. We are particularly grateful to Prof. Helen M. Burt for use of her laboratory facilities. The authors wish to acknowledge financial support by the A. P. Sloan Foundation (R.S.) and by the Natural Sciences and Engineering Research Council of Canada (NSERC). T.C.P. acknowledges NSERC for the provision of a fellowship. Allocation of CPU time on WestGrid facilities is gratefully acknowledged.

Supporting Information Available: Experimental procedure and methods for the preparation of the nanoshells. This material is available free of charge *via* the Internet at http://pubs.acs.org.

REFERENCES AND NOTES

1. Hirsch, L. R.; Stafford, R. J.; Bankson, J. A.; Sershen, S. R.; Rivera, B.; Price, R. E.; Hazle, J. D.; Halas, N. J.; West, J. L. Nanoshell-Mediated Near-Infrared Thermal Therapy of Tumors under Magnetic Resonance Guidance. *Proc. Natl. Acad. Sci. U.S.A.* **2003**, *100*, 13549–13554.
2. O'Neal, D. P.; Hirsch, L. R.; Halas, N. J.; Payne, J. D.; West, J. L. Photo-Thermal Tumor Ablation in Mice Using Near Infrared-Absorbing Nanoparticles. *Cancer Lett.* **2004**, *209*, 171–176.
3. Loo, C.; Lowery, A.; Halas, N.; West, J.; Drezek, R. Immunotargeted Nanoshells for Integrated Cancer Imaging and Therapy. *Nano Lett.* **2005**, *5*, 709–711.
4. Liu, Z. X.; Song, H. W.; Yu, L. X.; Yang, L. M. Fabrication and Near-Infrared Photothermal Conversion Characteristics of Au Nanoshells. *Appl. Phys. Lett.* **2005**, *86*, 113109.
5. Pissuwan, D.; Valenzuela, S.; Cortie, M. B. Therapeutic Possibilities of Plasmonically Heated Gold Nanoparticles. *Trends Biotechnol.* **2006**, *24*, 62–67.
6. Lal, S.; Clare, S. E.; Halas, N. J. Nanoshell-Enabled Photothermal Cancer Therapy: Impending Clinical Impact. *Acc. Chem. Res.* **2008**, *41*, 1842–1851.
7. Loo, C.; Lin, A.; Hirsch, L.; Lee, M.; Barton, J.; Halas, N.; West, J.; Drezek, R. Nanoshell-Enabled Photonics-Based Imaging and Therapy of Cancer. *Technol. Cancer Res. Treat.* **2004**, *3*, 33–40.
8. Wang, Y.; Xie, X.; Ku, G.; Gill, K. L.; O'Neal, D. P.; Stoica, G.; Wang, L. V. Photoacoustic Tomography of a Nanoshell Contrast Agent in the *In Vivo* Rat Brain. *Nano Lett.* **2004**, *4*, 1689–1692.
9. Wu, C. F.; Liang, X. P.; Jiang, H. B. Metal Nanoshells as a Contrast Agent in Near-Infrared Diffuse Optical Tomography. *Opt. Commun.* **2005**, *253*, 214–221.
10. Sershen, S. R.; Westcott, S. L.; Halas, N. J.; West, J. L. Temperature-Sensitive Polymer−Nanoshell Composites for Photothermally Modulated Drug Delivery. *J. Biomed. Mater. Res.* **2000**, *51*, 293–298.
11. Bikram, M.; Gobin, A. M.; Whitmire, R. E.; West, J. L. Temperature-Sensitive Hydrogels with SiO_2−Au Drug Delivery. *J. Controlled Release* **2007**, *123*, 219–227.
12. Troutman, T. S.; Leung, S. J.; Romanowski, M. Light-Induced Content Release from Plasmon-Resonant Liposomes. *Adv. Mater.* **2009**, *21*, 1–5.
13. Oldenburg, S. J.; Westcott, S. L.; Averitt, R. D.; Halas, N. J. Surface Enhanced Raman Scattering in the Near Infrared Using Metal Nanoshell Substrates. *J. Chem. Phys.* **1999**, *111*, 4729–4735.
14. Jackson, J. B.; Westcott, S. L.; Hirsch, L. R.; West, J. L.; Halas, N. J. Controlling the Surface Enhanced Raman Effect *via* the Nanoshell Geometry. *Appl. Phys. Lett.* **2003**, *82*, 257–259.
15. Talley, C. E.; Jackson, J. B.; Oubre, C.; Grady, N. K.; Hollars, C. W.; Lane, S. M.; Huser, T. R.; Nordlander, P.; Halas, N. J. Surface-Enhanced Raman Scattering from Individual Au Nanoparticles and Nanoparticle Dimer Substrates. *Nano Lett.* **2005**, *5*, 1569–1574.
16. Le, F.; Brandl, D. W.; Urzhumov, Y. A.; Wang, H.; Kundu, J.; Halas, N. J.; Aizpurua, J.; Nordlander, P. Metallic Nanoparticle Arrays: A Common Substrate for Both Surface-Enhanced Raman Scattering and Surface-Enhanced Infrared Absorption. *ACS Nano* **2008**, *2*, 707–718.

17. Averitt, R. D.; Sarkar, D.; Halas, N. J. Plasmon Resonance Shifts of Au-Coated Au_2S Nanoshells: Insight into Multicomponent Nanoparticle Growth. *Phys. Rev. Lett.* **1997**, *78*, 4217–4220.
18. Oldenburg, S. J.; Averitt, R. D.; Westcott, S. L.; Halas, N. J. Nanoengineering of Optical Resonances. *Chem. Phys. Lett.* **1998**, *288*, 243–247.
19. Oldenburg, S. J.; Jackson, J. B.; Westcott, S. L.; Halas, N. J. Infrared Extinction Properties of Gold Nanoshells. *Appl. Phys. Lett.* **1999**, *75*, 2897–2899.
20. Pham, T.; Jackson, J. B.; Halas, N. J.; Lee, T. R. Preparation and Characterization of Gold Nanoshells Coated with Self-Assembled Monolayers. *Langmuir* **2002**, *18*, 4915–4920.
21. Aden, A. L.; Kerker, M. Scattering of Electromagnetic Waves from Two Concentric Spheres. *J. Appl. Phys.* **1951**, *22*, 1242–1246.
22. Wang, H.; Goodrich, G. P.; Tam, F.; Oubre, C.; Nordlander, P.; Halas, N. J. Controlled Texturing Modifies the Surface Topography and Plasmonic Properties of Au Nanoshells. *J. Phys. Chem. B* **2005**, *109*, 11083–11087.
23. Mie, G. Beiträge zur Optik Trüber Medien Speziell Kolloidaler Metallösungen. *Ann. Phys.* **1908**, *25*, 377–445.
24. Kreibig, U.; Quinten, M.; Schoenauer, D.; Genzel, L. Optical Absorption Spectra of Pairs of Small Metal Particles. *Surf. Sci.* **1985**, *156*, 741–750.
25. Kreibig, U.; Quinten, M. Optical Properties of Aggregates of Small Metal Particles. *Surf. Sci.* **1986**, *172*, 557–577.
26. Storhoff, J. J.; Lazarides, A. A.; Mucic, R. C.; Mirkin, C. A.; Letsinger, R. L.; Schatz, G. C. What Controls the Optical Properties of DNA-Linked Gold Nanoparticle Assemblies? *J. Am. Chem. Soc.* **2000**, *122*, 4640–4650.
27. Rooney, P.; Rezaee, A.; Xu, S.; Manifar, T.; Hassanzadeh, A.; Podoprygorina, G.; Böhmer, V.; Rangan, C.; Mittler, S. Control of Surface Plasmon Resonances in Dielectrically Coated Proximate Gold Nanoparticles Immobilized on a Substrate. *Phys. Rev. B* **2008**, *77*, 235446.
28. Draine, B. T.; Flateau, P. J. *User Guide for the Discrete Dipole Approximation DDSCAT. 7.0*; http://arXiv.org/abs/0809.0337v5, **2008**.
29. Draine, B. T.; Flatau, P. J. Discrete-Dipole Approximation for Scattering Calculations. *J. Opt. Soc. Am. A* **1994**, *11*, 1491–1499.
30. Lynch, D. W.; Hunter, W. R. In *Handbook of Optical Constants of Solids*; Palik, E. D., Ed.; Academic Press: New York, 1985.
31. Malinsky, M. D.; Kelly, K. L.; Schatz, G. C.; Van Duyne, R. P. Nanosphere Lithography: Effect of Substrate on the Localized Surface Plasmon Resonance Spectrum of Silver Nanoparticles. *J. Phys. Chem. B* **2001**, *105*, 2343–2350.
32. Knight, M. W.; Wu, Y.; Lassiter, J. B.; Nordlander, P.; Halas, N. J. Substrates Matter: Influence of an Adjacent Dielectric on an Individual Plasmonic Nanoparticle. *Nano Lett.* **2009**, *9*, 2188–2192.
33. Van Helden, A. K.; Jansen, J. W.; Vrij, A. Preparation and Characterization of Spherical Monodisperse Silica Dispersions in Nonaqueous Solvents. *J. Colloid Interface Sci.* **1981**, *81*, 354–368.
34. Mayergoyz, I. D.; Fredkin, D. R.; Zhang, Z. Electrostatic (Plasmon) Resonances in Nanoparticles. *Phys. Rev. B* **2005**, *72*, 155412.
35. Brandl, D. W.; Mirin, N. A.; Nordlander, P. Plasmon Modes of Nanosphere Trimers and Quadrumers. *J. Phys. Chem. B* **2006**, *110*, 12302–12310.
36. Urzhumov, Y. A.; Shvets, G.; Fan, J.; Capasso, F.; Brandl, D.; Nordlander, P. Plasmonic Nanoclusters: A Path towards Negative-Index Metafluids. *Opt. Express* **2007**, *15*, 14129–14145.
37. Prodan, E.; Radloff, C.; Halas, N. J.; Nordlander, P. A Hybridization Model for the Plasmon Response of Complex Nanostructures. *Science* **2003**, *302*, 419–422.
38. Starov, V. M.; Velarde, M. G.; Radke, C. J. *Wetting and Spreading Dynamics*; CRC Press: Boca Raton, FL, 2007.
39. Zhang, L.; Persaud, R.; Madey, T. E. Ultrathin Metal Films on a Metal Oxide Surface: Growth of Au on TiO_2(110). *Phys. Rev. B* **1997**, *56*, 10549–10557.
40. Li, Q.; Rudolph, V.; Peukert, W. London−van der Waals Adhesiveness of Rough Particles. *Powder Technol.* **2006**, *161*, 248–255.
41. Heuberger, M.; Tresch, S.; Dietler, G. Nucleation and Growth of Gold on Polypyrrole Investigated by Quantitative XPS and STM. *Thin Solid Films* **1995**, *271*, 144–146.
42. Stöber, W.; Fink, A.; Bohn, E. Controlled Growth of Monodisperse Silica Spheres in Micron Size Range. *J. Colloid Interface Sci.* **1968**, *26*, 62–69.
43. Westcott, S. L.; Oldenburg, S. J.; Lee, T. R.; Halas, N. J. Formation and Adsorption of Clusters of Gold Nanoparticles onto Functionalized Silica Nanoparticle Surfaces. *Langmuir* **1998**, *14*, 5396–5401.
44. Duff, D. G.; Baiker, A.; Edwards, P. P. A New Hydrosol Formation of Gold Clusters. 1. Formation and Particle Size Variation. *Langmuir* **1993**, *9*, 2301–2309.
45. Duff, D. G.; Baiker, A.; Gameson, I.; Edwards, P. P. A New Hydrosol Formation of Gold Clusters. 2. A Comparison of Some Different Measurement Techniques. *Langmuir* **1993**, *9*, 2310–2317.